Engineering Failure Analysis 166 (2024) 108891

Contents lists available at ScienceDirect

Engineering Failure Analysis

journal homepage: www.elsevier.com/locate/engfailanal

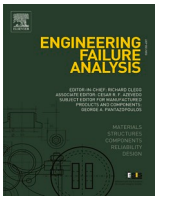

# Evaluation of stress-assisted corrosion performance of L-PBF processed Ti6Al4V: A microcapillary electrochemical approach

Arshad Yazdanpanah *, Nicolò Capuzzo, Mona Khodabakhshi, Manuele Dabalà

*Department of Industrial Engineering, University of Padova, Via Marzolo 9, 35131 Padova, Italy*

ARTICLE INFO

*Keywords:*
Additive manufacturing
Ti6Al4V alloy
Corrosion
Microcapillary technique
Electrochemical behaviour

ABSTRACT

This study investigated the corrosion behaviour of Ti6Al4V alloy fabricated using the Laser Powder Bed Fusion (L-PBF) additive manufacturing technique, comparing its performance to conventionally manufactured counterparts. The microcapillary electrochemical method effectively detected even slight changes in corrosion response for both materials under various conditions, including tensile straining, surface roughness, and presence of fluoride ions. Under tensile strain, the L-PBF alloy's finer grain size and submicron martensitic structure further enhanced its corrosion performance. High fluoride ion concentrations intensified corrosion, with conventional Ti6Al4V exhibiting greater susceptibility to pitting. Notably, both materials displayed exceptional resistance to stress corrosion cracking.

## 1. Introduction

Due to the need for a biocompatible, corrosion-resistant, and mechanically robust materials in the harsh oral environment, titanium alloys, particularly Ti6Al4V have become the basis for dental implants [1]. Their excellent osseointegration potential, stemming from biocompatibility, allows for strong bonding with bone tissue [2]. Furthermore, the high strength-to-weight ratio of Ti6Al4V ensures sufficient mechanical capabilities to withstand biting and chewing forces without compromising weight in the jawbone [3]. The microstructure of Ti6Al4V alloy plays a crucial role in its performance as a dental implant. At room temperature, this titanium alloy typically exhibits a two-phase ($\alpha + \beta$) microstructure. The primary phase is the hexagonal close-packed (HCP) α-phase, which offers good biocompatibility and corrosion resistance [4]. The secondary phase is the body-centred cubic (BCC) β-phase, which contributes to the alloy's overall strength. The relative volume fraction and morphology (shape and distribution) of these phases can be influenced by thermo-mechanical processing techniques, and this in turn can affect the mechanical properties of the implant [1]. For instance, a higher volume fraction of the α-phase might enhance biocompatibility, while a greater β-phase content could improve strength [5]. Optimizing the microstructure through processing techniques is crucial to achieve the desired balance between biocompatibility, strength, and corrosion resistance for successful dental implant applications [6].

Metal additive manufacturing (MAM) has emerged as a transformative technology for dental implant production, surpassing traditional subtractive methods [7]. Laser Powder Bed Fusion (L-PBF) is a particularly leading MAM technique in this domain. L-PBF employs a high-powered laser beam to selectively melt and fuse metallic powder particles layer-by-layer, constructing a three-dimensional implant based on a CAD file [8]. This technology offers compelling advantages for dental implants [9]. Firstly, L-PBF facilitates the design of intricate, patient-specific implants with complex surface features that promote osseointegration. Unlike

* Corresponding author.
*E-mail address:* arshad.yazdanpanah@phd.unipd.it (A. Yazdanpanah).

https://doi.org/10.1016/j.engfailanal.2024.108891
Received 12 July 2024; Received in revised form 28 August 2024; Accepted 16 September 2024
Available online 18 September 2024

traditional methods restricted to pre-manufactured stock, L-PBF enables customization to precisely match individual bone anatomy. Secondly, the precise control inherent to L-PBF allows for the creation of porous internal structures within the implant [10]. Mimicking the natural bone structure, these pores encourage bone ingrowth, further enhancing osseointegration. Lastly, L-PBF promotes material efficiency by utilizing only the necessary amount of material during the build process, minimizing waste compared to subtractive methods [6]. This is particularly advantageous for expensive materials like titanium alloys used in dental implants.

The rapid solidification rates inherent to L-PBF typically result in a non-equilibrium microstructure compared to conventionally processed Ti6Al4V [11]. As-built L-PBF parts often exhibit a dominant presence of the metastable α' (acicular martensite) phase, a transformation product of the high-temperature β-phase due to rapid cooling [12]. This α' phase can offer good biocompatibility, but its needle-like morphology might raise concerns about long-term mechanical stability [12]. Traces of retained β-phase or a transformed α + β mixed phase assemblage might also be present depending on the specific processing parameters.

The long-term viability of Ti6Al4V dental implants centres on their ability to resist corrosion and stress corrosion cracking (SCC) within the complex oral environment. Corrosion, the gradual degradation of the implant material by bodily fluids and oral bacteria, can compromise implant integrity and potentially lead to catastrophic fracture. SCC, a specific form of corrosion, is triggered by the synergistic action of a tensile stress (from biting forces) and a corrosive environment [13]. This can accelerate crack formation and pose a significant life hazard due to potential implant failure.

Despite the widespread adoption of L-PBF-processed Ti6Al4V for dental implants, concerns regarding its corrosion behaviour compared to conventional counterparts persist. Research findings on the relative corrosion resistance of these materials are contrary [14–16]. Several studies have investigated the influence of processing techniques on the corrosion behaviour of Ti-6Al-4V for dental applications. Chiu et al. [17] evaluated the performance of L-PBF processed alloys in Ringer's solution, demonstrating that L-PBF process parameters can alter the bulk metal, enhancing its resistance to corrosive ions. In contrast, Chen et al. [18] reported a higher dissolution rate of metal ions in dynamic Hank's solution for the additive manufactured material compared to conventional counterpart, leading to the formation of ionic Ti and oxygen vacancies. This resulted in a higher density of oxygen vacancies and a higher oxygen diffusion coefficient within the passive film. Dai et al. [19] compared the corrosion resistance of L-PBF produced Ti-6Al-4 V samples with commercially available Grade 5 alloys. Their findings suggest that the SLM process might lead to inferior corrosion resistance. This was attributed to the presence of a lower β-Ti phase and a larger α'-Ti phase in the SLM-produced microstructure compared to the conventional counterpart. Tamilselvi et al. [20] observed the formation of a similar single passive layer on both L-PBF and conventionally processed alloys after immersion in SBF for 360 h, as indicated by EIS measurements, while Chen et al. [21] reported superior performance of the conventional alloy compared to its L-PBF counterpart in 3.5 % sodium chloride solution. This difference was attributed to the distinct phase compositions of the L-PBF material.

While extensive research has explored the corrosion behaviour of L-PBF-processed Ti6Al4V, contradictory results persist in the literature. This variability can be attributed, in part, to the inherent sensitivity of the L-PBF process to parameters like laser power and scan speed, which significantly influence the resulting microstructure[11]. Notably, L-PBF-processed Ti6Al4V often exhibits a higher α' phase content and potential micro-cracks or porosities, both of which are known to affect corrosion resistance [13,15,16]. Furthermore, a critical gap exists in our understanding of how loading conditions influence the corrosion behaviour of L-PBF Ti6Al4V for dental implants. Conventional polarization techniques, which expose large surface areas, can obscure the influence of microstructural features on corrosion. The destructive nature of these techniques requires new samples for each experiment, introducing variability. Microcapillary techniques, allowing repeated measurements on the same surface, can improve reliability. Additionally, conventional methods often struggle to detect early-stage corrosion due to their reliance on large surface areas. This technique allows for the targeted examination of smaller areas, offering a promising approach for identifying subtle changes in the submicron structural state of materials. [22–28].

The current investigation aims to clarify the comparability of the corrosion performance of L-PBF processed alloy Ti6Al4V with conventionally produced counterpart under tensile loading state. The prophylactic use of fluoride-containing products, such as toothpaste, mouthwashes, and gels, is a cornerstone of dental caries prevention. However, the potential for fluoride-induced corrosion of titanium alloy dental implants in the oral environment remains a subject of interest, given the variability in fluoride concentrations and pH of these products. To mimic the clinical context of dental implant placement, our study employed simulated body fluid (SBF) as a corrosion medium. This choice reflects the direct contact of dental implants with bone, a physiological environment similar to that of body implants. The potential for fluoride contamination at the implant-bone interface, particularly in cases of gum recession, poses a significant concern. In order to be able to detect even slight variations microcapillary electrochemical polarization techniques were used which has shown its high accuracy and sensitivity to even slight alterations in corrosion studies under tensile loading state. Various microstructural techniques were used to identify the morphology of the corrosion defects and the microstructural features of the specimens.

## 2. Experimental Procedure

### *2.1. L-PBF specimen preparation*

Cubic specimens (30 × 10 × 30 mm) were fabricated using EOS M100 L-PBF machine equipped with a 200 W fibre laser. Cubes were built directly on the build platform without support structures, utilizing a laser spot diameter of 50 μm. The feedstock consisted of gas-atomized, surgical-grade Ti-6Al-4 V powder with a particle size range of 15–45 μm. An inert, high-purity argon atmosphere was maintained within the build chamber to minimize oxygen contamination. A layer thickness of 0.05 mm was chosen to balance productivity with desired material properties. To achieve the highest possible density in the fabricated specimens, the LPBF process

parameters employed in this study adhered to the standard recommendations provided by the equipment manufacturer. These parameters are not disclosed here due to their proprietary nature. Furthermore, conventionally produced identical material was also used for comparative study in this investigation.

Following fabrication, the specimens were sectioned using electro discharge machining (EDM) to a thickness of 0.8 mm, oriented perpendicular to the build direction. To minimize the influence of surface roughness and the EDM process itself, careful grinding and polishing with different grit sizes of 1200, and up to 1 μm colloidal silica suspension were employed in order to study the effect of surface roughness on corrosion performance of the materials. To minimize variations in surface roughness, each specimen was prepared using a new grinding paper under identical grinding conditions. Subsequently, the samples were ultrasonically cleaned in 70 % ethanol for 5 min, followed by rinsing with pure ethanol. Finally, the samples were left undisturbed under ambient conditions for 48 h to allow for native oxide layer formation and the stabilization of any surface modifications introduced during metallographic preparation. Due to the small test area required by the microcapillary technique, all experiments were conducted on the same specimen, effectively controlling for any potential alterations in surface roughness.

### 2.2. Micro and submicron structural analysis

A comprehensive analysis was conducted to characterize the microstructure of the specimens before and after electrochemical polarization experiments. Pore morphology was investigated using an optical microscope at magnifications of 5x, 10x, and 20x. A total of 30 images were captured across all magnification levels for each sample condition (as-built and post-polarization). For as-built specimens, Kroll's etchant solution was employed to reveal the microstructure. Following the electrochemical polarization experiments, the samples were subjected to a thorough cleaning protocol to remove any residual electrolyte or corrosion products. This involved a 15-minute ultrasonic cleaning step in 70 % ethanol, followed by a final rinse with pure ethanol. A high-resolution field emission SEM (FE-SEM) FEI QUANTA 250 equipped with an energy-dispersive X-ray spectroscopy (EDS) detector was utilized for further characterization of the as-built microstructure.

### 2.3. Electrochemical polarization assessment utilizing microcapillary technique

The primary objective of the current study was to compare the corrosion and electrochemical performance of L-PBF processed materials with those produced by conventional methods. To ensure the validity of this comparison, the environmental conditions across all experiments were carefully controlled to remain as consistent as possible. This methodological approach was intended to highlight the inherent differences between the materials, minimizing the influence of environmental and topographical factors. To enhance the reliability of the reported results, each experiment was conducted minimum three times, resulting in a standard deviation of 2 %. This statistical analysis confirms the consistency and reproducibility of the experimental data.

It is important to note that the bioactivity of the materials under investigation was beyond the scope of this study. Typically, experiments conducted at 37 °C aim to evaluate a material's bioactivity, which involves its ability to bond with living bone. In such cases, immersion in SBF can lead to the formation of a bone-like apatite layer on the surface of bioactive materials, indicating their potential for successful osseointegration (the process by which an implant integrates with bone tissue). While the assessment of bioactivity, including the kinetics of osseointegration and the comparison between L-PBF materials and their conventional counterparts, is indeed an important and valuable area of research, it constitutes a separate topic that merits further investigation.

#### 2.3.1. Electrochemical polarization experiments in as built state

A microcapillary electrochemical cell with a tip diameter of 500 μm (corresponding to a surface area of 0.19625 $mm^2$) was employed to enhance the sensitivity towards subtle surface alterations during corrosion testing. This high-resolution technique facilitates the targeted analysis of specific areas on the sample surface. A conventional three-electrode configuration was utilized, comprising a saturated calomel electrode (SCE) as the reference, a platinum wire counter electrode (0.3 mm diameter), and the sample itself as the working electrode. The schematic of the microcapillary setup is presented in Fig. 1.

The tip of the microcapillary was sealed with silicon to ensure the elimination of crevice corrosion in the interface of the capillary

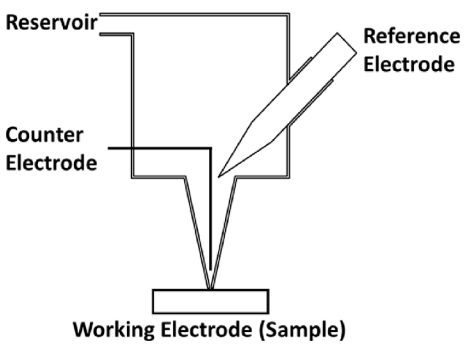


**Fig. 1.** Schematic of the microcapillary electrochemical cell.

tip with the surface. A Gamry 1001 interface potentiostat was used for all experiments, with data acquisition and analysis facilitated by the manufacturer's dedicated software. Specimens (with a dimension of 30 × 10 × 0.8 mm) were pre-treated by immersion in a SBF solution with a composition shown in Table 1 for 30 min before performing polarization measurements. It's important to note that electrochemical impedance spectroscopy (EIS) was performed on a separate, masked area (diameter of 5 mm) using a standard setup, independent of the microcapillary cell. For EIS experiments a frequency range between 1 mHz and 100 kHz was used by performing the experiment at OCP value obtained prior to experiment with an AC amplitude of 10 mV.

To investigate the behaviour of the passive oxide layer, various direct current polarization techniques were employed, including potentiodynamic, galvanostatic, and potentiostatic methods. Potentiodynamic polarization scans were conducted in the range of −0.5 to 1.5 V with respect to OCP value with a scan rate of 2 $mV.s^{-1}$. To mitigate the accumulation of aggressive ions and corrosion products near the microcapillary test area, higher scan rates were employed for the potentiodynamic polarization measurements, exceeding those commonly used. The smaller surface area in contact with the solution, coupled with the stationary and closed-loop nature of the microcapillary method, makes these tests particularly susceptible to alterations in normal conditions due to prolonged anodic polarization. Additionally, to avoid the electrochemical effects of water electrolysis (which can occur at potentials exceeding 1.2 V in aqueous solutions) the potential range in this comparative study was restricted to 1.5 V relative to the OCP value. Conversely, potentiostatic polarization involved maintaining a constant potential set at the breakdown potential identified from the prior potentiodynamic measurements. Galvanostatic polarization was carried out at a constant current density corresponding to the transpassive region identified in the potentiodynamic data.

#### *2.3.2. Electrochemical polarization under tensile loading state*

Microcapillary electrochemical polarization experiments were utilized to simulate the combined effect of tensile strain and a fluoride-contaminated environment, replicating the conditions experienced by dental implants in the oral cavity. Specimens were subjected to tensile strain while immersed in a SBF solution with 2.5 % sodium fluoride (NaF) to mimic the presence of fluoride ions in the oral environment. This level surpasses the maximum concentration allowed in commercial toothpaste (1500 ppm) and is comparable to the high fluoride content found in professional dental varnishes. Given the potential for localized fluoride accumulation, particularly in areas where dental varnishes are applied, this concentration was chosen to assess the worst-case scenario. The resulting fluoride-enriched SBF exhibited a pH of 4.2, indicating its acidic nature. This acidic environment can enhance the corrosive potential of fluoride on titanium alloys.

It is well documented that titanium alloys exhibit heightened susceptibility to localized corrosion attacks in fluoride-rich environments [29–34]. To isolate the influence of microstructural features on the observed behaviour, experiments were conducted exclusively on carefully polished surfaces using a 1 μm silica suspension. This approach minimizes the impact of surface finish variations and ensures a consistent surface morphology across all specimens. The applied strain level corresponded to a maximum 0.2 % of the material's yield stress (0.2 % proof stress). A high-precision strain gauge system DT9829 (Measurement Computing Corporation, USA), configured in a half Wheatstone bridge arrangement, was employed for accurate strain measurement during tensile loading.

Additionally, to assess the influence of constant current and potential on the oxide layer, two separate sets of electrochemical measurements were conducted. To further evaluate the resistance of the passive layer formed on the samples in the aggressive environment, microcapillary galvanostatic polarization tests were employed. A constant current density of 100$nA.mm^{-2}$ was applied across all experiments to ensure a focused assessment within the passivation regime. Additionally, tensile straining was implemented at various levels, ranging from no strain up to the 0.2 % proof strain. This approach aimed to elucidate the material's behaviour under diverse loading states while remaining below the yield limit.

## 3. Results and discussion

### *3.1. Micro and submicron structural analysis*

Microstructural analysis as shown in Fig. 2 reveals distinct microstructural features between conventionally produced and L-PBF-processed Ti6Al4V samples. The conventional alloy displayed a typical biphasic microstructure consisting of equiaxed α-phase grains dispersed within a β-phase matrix. The β-phase, stabilized by vanadium, remains present at room temperature due to its higher stability at elevated temperatures [35]. In contrast, L-PBF samples exhibited a microstructure dominated by the presence of a metastable α' (martensitic) phase. This transformation arises from the rapid solidification rates associated with the L-PBF process [12,36]. The high

**Table 1**
Composition of simulated body fluid used in the current investigation.

| | |
|---|---|
| NaCl | 6.8 g/L |
| $CaCl_2$ | 0.2 g/L |
| KCl | 0.4 g/L |
| $MGSO_4$ | 0.1 g/L |
| $NaHCO_3$ | 2.2 g/L |
| $Na_2HPO_4$ | 0.126 g/L |
| $NaHPO_4$ | 0.026 g/L |

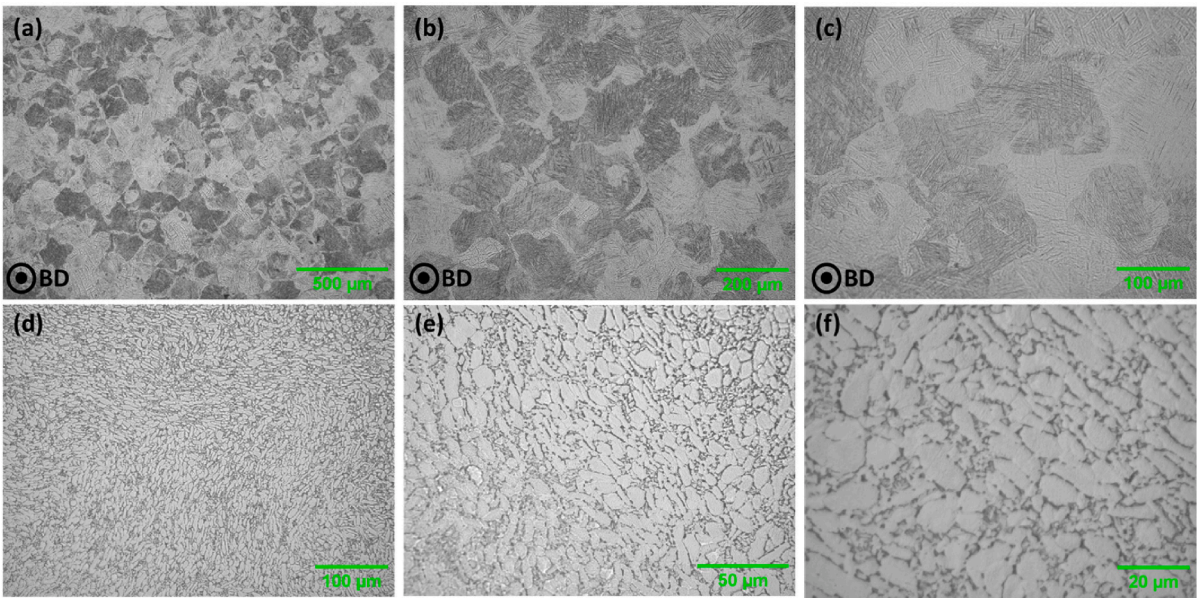


**Fig. 2.** Optical microstructural analysis at various magnifications for (a), (b), and (c) L-PBF processed alloy Ti6Al4V, and (d), (e), and (f) conventional counterpart. BD is corresponding to build direction of L-PBF specimens.

thermal gradients created by the laser beam result in a rapid quenching, leading to the formation of α' phase instead of the equilibrium α-phase observed in the conventional material. These α' phase grains appear as thin, needle-like structures grouped into distinct islands within the microstructure (Fig. 2b, and c).

The size of these α' phase needles is generally significantly smaller than the α-phase grains observed in the conventional alloy.

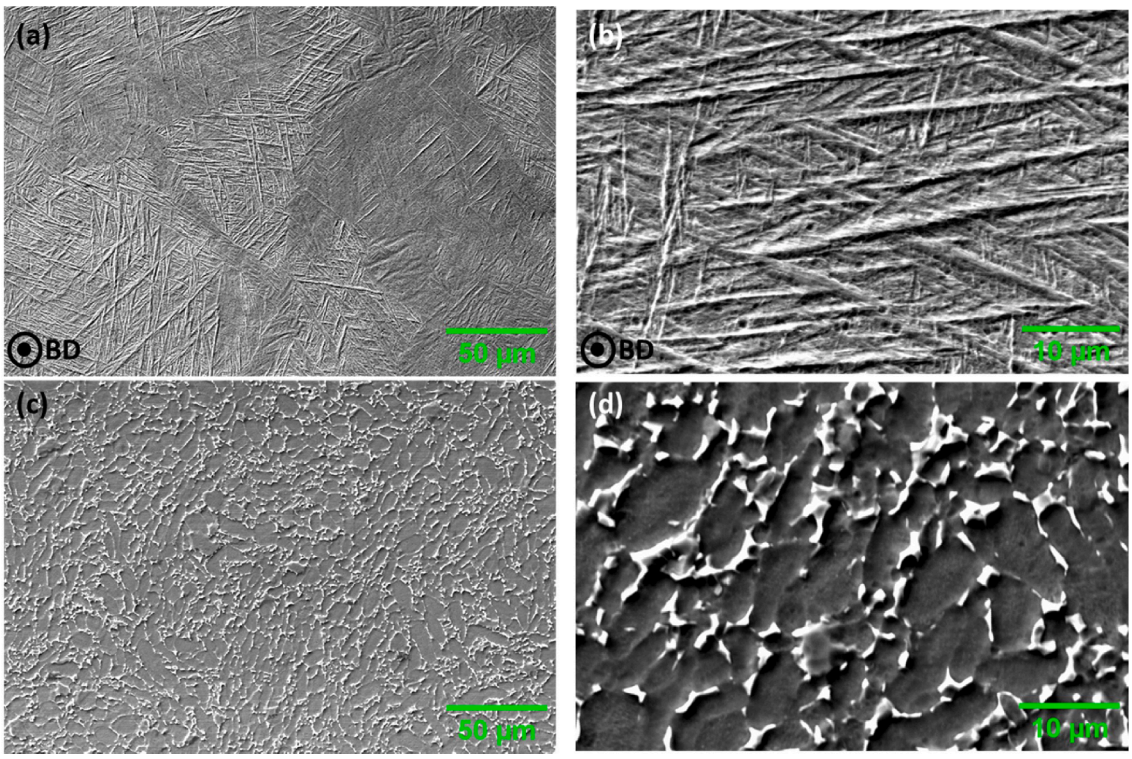


**Fig. 3.** SEM analysis of (a), and (b) L-PBF processed alloy Ti6Al4V, and (c), and (d) conventional counterpart. BD is corresponding to build direction of L-PBF specimens.

Furthermore, the α' phase exhibits a localized texture, with similar grain orientation within each island but differing orientations across different islands. This localized texture reflects the heat flow patterns during laser melting, with subsequent laser passes potentially influencing the orientation of newly formed α' phase grains [37]. The L-PBF image (Fig. 2a) visually demonstrates the influence of the laser path. The sequential arrangement of α' phase islands aligns with the laser scanning direction, while the remaining β-phase preferentially accumulates at the island boundaries. SEM analysis as shown in Fig. 3 further corroborates the presence of the α' (martensitic) phase in L-PBF samples. The laser beam creates a localized thermal gradient, influencing the solidification process and the subsequent crystallographic orientation of the α' phase. As subsequent laser passes melt adjacent areas, the resulting α' phase needles may have a different orientation due to the slightly altered thermal profile [37].

### 3.2. Microcapillary electrochemical polarization

#### 3.2.1. Open circuit potential

Open circuit potential (OCP) measurements were conducted on all samples to assess their initial corrosion behaviour in SBF solution. OCP is a fundamental parameter that reflects the tendency of a material to undergo electrochemical reactions at the electrode/electrolyte interface. After a one-hour stabilization period (shown in Fig. 4), all OCP curves reaches a steady state, indicating the establishment of a stable electrochemical equilibrium. Notably, all samples exhibited negative OCP values, confirming their susceptibility to corrosion in the SBF environment. Materials with more positive OCP values are generally considered more corrosion resistant as their atoms are less prone to oxidation and dissolution [38].

Interestingly, the OCP measurements revealed a key difference between the L-PBF and conventional samples. For both surface roughness levels (1 μm and 1200 Grit), the L-PBF samples consistently exhibit higher OCP values compared to their conventional counterparts (Fig. 4). This observation suggests a more noble behaviour of the L-PBF material, implying a lower dissolution rate in the SBF solution. This difference can be attributed to several factors. The presence of the α' phase in L-PBF samples might influence the formation and stability of the passive oxide layer on the surface, potentially leading to enhanced corrosion resistance compared to the β-phase dominant microstructure of conventional samples. Furthermore, the grain size in L-PBF specimens is significantly smaller compared to conventional counterpart leading to shorter diffusion path for the formation of a protective native oxide layer on the surface [39].

The final OCP values for polished samples (1 μm) of both L-PBF and conventional samples were found to be relatively close, with a difference of approximately 20 mV. This suggests a comparable corrosion behaviour for the polished surfaces of both materials. However, the OCP profiles provide further insights. Notably, the OCP curve for the L-PBF sample exhibited a smoother trend and reached stability more rapidly compared to the conventional sample. The average rate of change of the OCP curve over time was lower for the L-PBF sample (0.0579 mV/s) compared to the conventional sample (0.168 mV/s). These observations suggest that the passive oxide layer on the L-PBF surface forms more rapidly and with greater uniformity.

On the other hand, the OCP measurements for the 1200 Grit samples revealed a significant difference in their final OCP values. The L-PBF sample continued to exhibit a higher OCP compared to the conventional sample, further emphasizing the superior performance of the L-PBF surface passive layer under these conditions. This disparity highlights the importance of surface roughness in corrosion studies. Increased surface roughness leads to a larger exposed interfacial area, which can accelerate the corrosion process [40].

The formation of a passive layer on the surface of materials exposed to corrosive environments is a complex process driven by redox reactions [41]. Initially, oxidation reactions predominate, leading to the formation and densification of the passive layer. As the system evolves, an equilibrium between oxidation and reduction reactions is established (mixed potential theory) [42]. This equilibrium is highly dependent on the material's microstructure and the specific conditions of the corrosive environment. In materials that exhibit

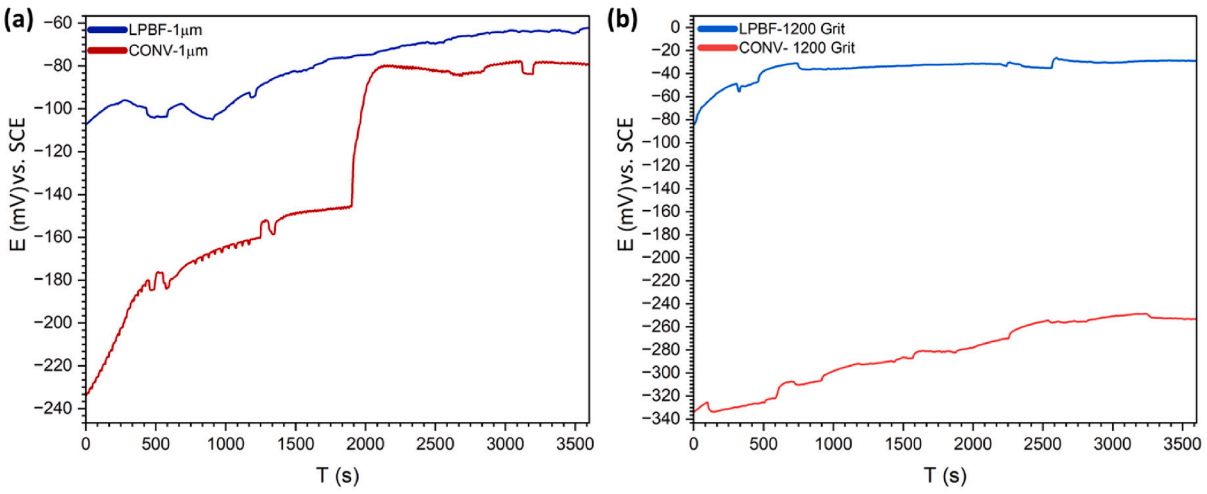


**Fig. 4.** OCP measurement of (a) for the polished specimens up to 1 μm silica suspension, and (b) for the 1200-grit size grinding.

multiple phases, localized galvanic coupling can occur, enhancing redox activity and potentially delaying the establishment of equilibrium [43]. This phenomenon can manifest as a more pronounced increase OCP over time, reflecting a scenario where the rate of oxidation (contributing to passive layer development) exceeds the rate of reduction at these localized sites.

### 3.2.2. Electrochemical impedance spectroscopy

The EIS analysis was employed to gain further insights into the corrosion behaviour of the samples at the electrode/electrolyte interface. The analysis revealed distinct differences in the response of 1 μm polished and 1200 Grit samples as shown in Fig. 5, highlighting the interplay between surface finish and microstructure. The EIS results, particularly the observed phase shifts and time constants in the Bode plots, suggest variations in the electrical properties of the electrode/electrolyte interface for each sample. L-PBF

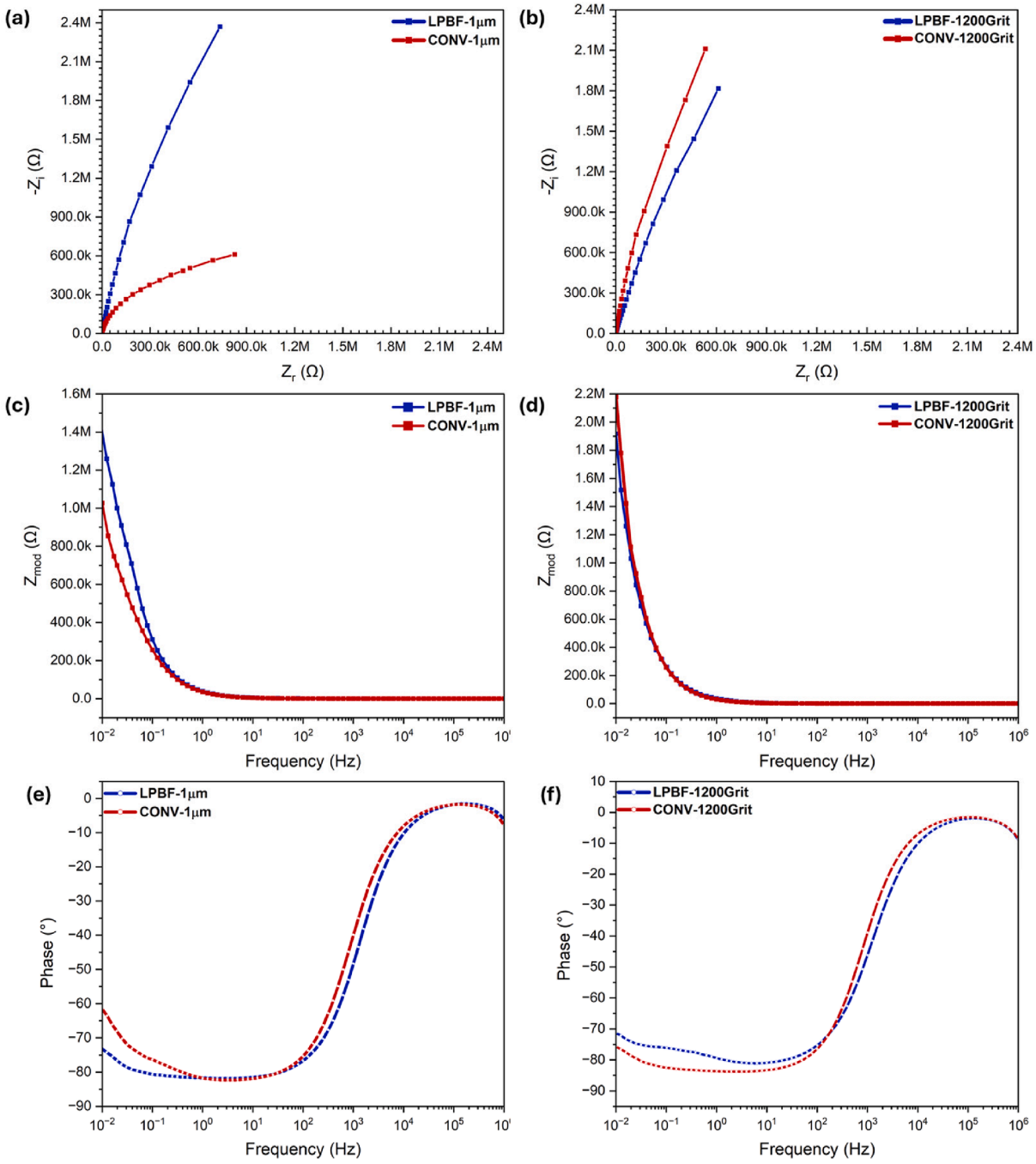


**Fig. 5.** Bode and Nyquist EIS representation of (a), and (c) polished up to 1 μm, and (b), and (d) for the specimens polished with 1200 grit size.

specimens in general revealed higher resistance toward faradaic reactions for both 1 μm and 1200-Grit cases indicating significantly better performance of the passive layer toward the anodic reactions.

Furthermore, rougher surfaces (1200 Grit) possess a larger exposed area compared to polished surfaces (1 μm). This increased area significantly impacts the overall impedance response measured by EIS. Additionally, rough surfaces often exhibit greater heterogeneity, with variations in surface features like peaks and valleys. These variations can influence the distribution of the passive oxide layer and the underlying substrate, further affecting the overall impedance behaviour.

The observed differences between 1 μm polished L-PBF and conventional samples (Fig. 5a and c) suggest a potential influence of microstructure on the corrosion behaviour. The L-PBF samples exhibited a larger response in the Nyquist plots, indicating a potentially higher impedance to the faradaic reactions associated with corrosion. This suggests a more effective barrier to electron transfer processes at the metal/oxide interface in the L-PBF material. The underlying reasons for this enhanced performance might be related to the specific microstructure of L-PBF Ti6Al4V. The presence of the α' phase in L-PBF samples could influence the formation and composition of the passive oxide layer, potentially leading to improved barrier properties compared to the β-phase dominant microstructure of conventional samples.

The results from the 1200 Grit samples were less conclusive. This potentially indicates that for this surface roughness, the influence of surface finish might supress the microstructural differences between L-PBF and conventional samples. The increased surface area associated with the rougher finish can significantly complicate the interpretation of EIS data, making it challenging to isolate the specific contribution of the underlying microstructure. The results suggest that the L-PBF material exhibits a potentially superior corrosion resistance compared to the conventional material, particularly for smoother surfaces.

### 3.2.3. *Potentiodynamic polarization*

From the outcome of potentiodynamic polarization analysis shown in Fig. 6, for the 1 μm polished samples, the curves exhibited a smooth and continuous rise in current density from −0.6 V to 1.2 V, indicating a well-defined transition from the corrosion potential to the transpassive region. In contrast, the L-PBF polished up to 1200 grit sample displayed a distinct characteristic. Its curve exhibited numerous breakdown points followed by repassivation events at potentials exceeding 0.7 V. These sudden increases in current density suggest localized breakdown of the passive oxide layer on the rougher surface, followed by its reformation upon reaching a higher potential. The conventional polished sample up to 1200 grit also displayed irregularities, particularly at the boundaries between the anodic and cathodic branches of the curve. These irregularities might be attributed to a combination of factors related to the higher surface roughness. The rough surface likely possesses areas with varying degrees of passivity, leading to inconsistencies in the current response during the polarization scan. The deeper grooves and crevices on the rough surface can act as initiation sites for localized pitting corrosion [40]. The breakdown of the passive layer in these specific areas could contribute to the observed current spikes.

The observed differences in the polarization behaviour strongly support the notion that surface roughness plays a crucial role in corrosion susceptibility. The increased surface area associated with a rougher finish (1200 Grit) creates a larger area susceptible to localized corrosion phenomena. This is further supported by the corrosion current densities at a specific potential for each sample. The higher current densities observed for the 1200 Grit samples compared to their 1 μm counterparts indicate a more pronounced corrosion rate for the rougher surfaces. This aligns with the breakdown events observed in the L-PBF-1200Grit curve.

The corrosion potential (Ecorr) values obtained from the polarization curves further emphasize the importance of surface finish. For the 1 μm polished samples, the Ecorr values were very similar for both L-PBF and conventional materials, suggesting minimal differences in their initial susceptibility to corrosion at this specific surface condition. However, the Ecorr of the L-PBF-1200Grit sample was significantly higher compared to the conventional-1200Grit sample. This observation aligns with the OCP results, where the L-PBF material exhibited a higher tendency to resist corrosion even for the rougher surface finish. These findings highlight the

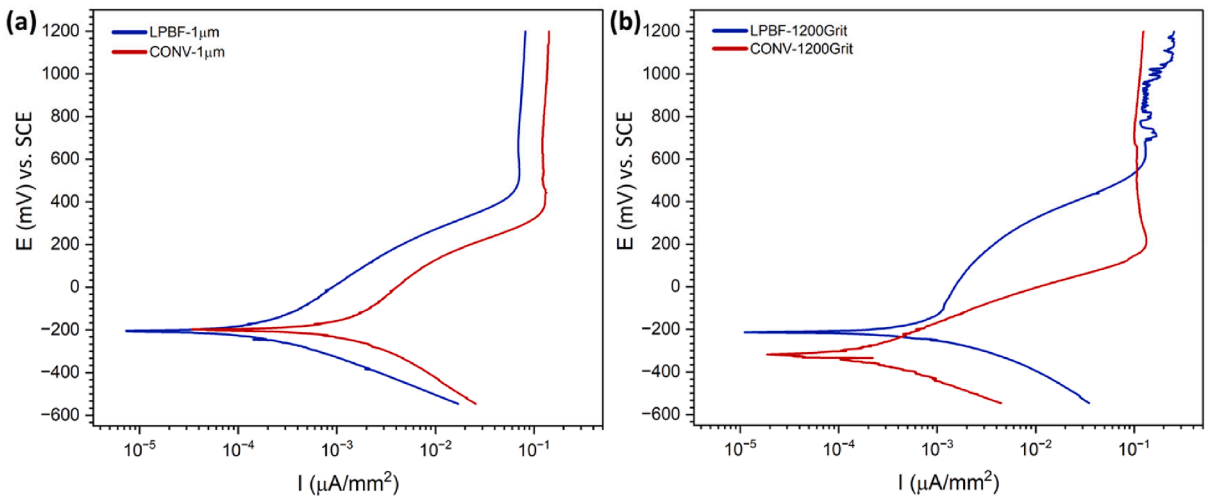


**Fig. 6.** Potentiodynamic polarization (a) for 1 μm polished specimens, and (b) 1200 grit size.

interplay between surface roughness and intrinsic corrosion resistance (related to microstructure) in determining the overall corrosion behaviour.

The 1 μm polished samples exhibited a well-defined passivation zone in their polarization curves (Fig. 6a), characterized by a vertical region around + 400 mV where the current density remains relatively constant. Interestingly, the current density in the passivation zone was consistently higher for the conventional-1 μm sample compared to the L-PBF-1 μm sample. This observation suggests that the passive layer formed on the L-PBF material exhibits superior resistance to the passage of current at a similar potential and the L-PBF material passivates more effectively, leading to a lower corrosion rate under these conditions.

Furthermore, the results suggest that the L-PBF material exhibits superior corrosion resistance compared to the conventional material, particularly for smoother surfaces. This enhanced performance can be attributed to both the intrinsic corrosion resistance associated with its microstructure and the effectiveness of the passive layer formed on its surface. The values for the key parameters obtained from potentiodynamic polarization results is summarized in Table 2.

### 3.2.4. Galvanostatic polarization

Galvanostatic polarization experiments were employed to further assess the corrosion resistance of the samples under a constant current density. The applied current density was chosen based on the values reached in the passivation zone of the potentiodynamic polarization curves. This approach allows for a focused evaluation of the material's behaviour within the passivation regime. The galvanostatic polarization test results for both 1 μm and 1200 Grit samples reveals a common trend as shown in Fig. 7. Regardless of the applied current density and the specific material (L-PBF or conventional), the electrode potential tended to stabilize at a similar level over time. This observation suggests comparable corrosion performance between the L-PBF and conventionally manufactured materials under the applied constant current conditions. This finding suggests that for a given applied current density within the passivity range, the overall corrosion rates of L-PBF and conventional materials could be comparable, irrespective of the surface finish.

To further explore the stability of the passive layer, the GS test was repeated under a significantly higher current density of 10 μA shown in Fig. 8. This deliberately harsh condition can potentially induce localized breakdown of the passive film. For the 1 μm polished samples, the stabilized potentials remained similar for both L-PBF and conventional materials, even under this extreme current density. This observation reinforces the notion of comparable corrosion resistance between the materials under these specific conditions.

However, the behaviour of the conventional samples differed significantly at both surface roughness levels when subjected to the 10 μA current density. The conventional samples exhibited frequent potential breakdowns after 500 s. Interestingly, the conventional-1 μm sample eventually recovered from these breakdowns and stabilized at a potential value close to the final value of the corresponding L-PBF sample. This suggests that while the conventional material might be more susceptible to localized breakdown of the passive layer under extreme current conditions, it might possess some degree of self-healing or repassivation capability. Despite the observed potential breakdowns in the conventional samples, a clear trend emerges from the galvanostatic polarization curves. Even under the extreme current density of 10 μA, the overall trend of the potential versus time curves for both materials appears to converge towards a common value. This suggests that both materials retain a certain level of passivity, even if the conventional material exhibits a less stable response initially.

However, a key difference lies in the breakdown behaviour. The passive layer formed on the L-PBF material appears to exhibit a more stable behaviour compared to the conventional material. This is particularly evident at the higher current density (Fig. 8). The L-PBF samples reached a steady state more rapidly and maintained it for a longer duration compared to their conventional counterparts. This observation suggests that the passive layer formed on the L-PBF material offers superior resistance to breakdown under constant current conditions, especially when challenged by harsher environments.

### 3.2.5. Potentiostatic polarization

Potentiostatic polarization tests were conducted to assess the stability of the passive layer formed on the samples under a constant applied potential. A potential of 1.5 V was chosen for all experiments to ensure operation within the passivation regime identified through the previous potentiodynamic polarization results (Fig. 6). The potentiostatic test results revealed key differences in the behaviour of L-PBF and conventional samples (Fig. 9), particularly at the 1 μm polished surface finish. For the L-PBF-1 μm sample, the current density curve exhibited a relatively smooth trend and reached a steady-state value, indicating stable passivation behaviour. This observation suggests that the L-PBF material's passive layer effectively resists breakdown under the applied constant potential.

In contrast, the current density curves for the conventional-1 μm samples displayed regions of instability. These fluctuations are indicative of cycles of breakdown and repassivation of the passive layer. This suggests a less stable passive layer on the conventional material, potentially susceptible to localized breakdown under the constant potential stress. The observed instability might be attributed to microstructural factors. The β-phase dominant microstructure of conventional samples might exhibit greater heterogeneity in the composition and properties of the passive layer compared to the L-PBF material. Furthermore, pre-existing defects or

**Table 2**
Results of potentiodynamic polarization experiments.

| Sample | $E_{corr}$ (mV) | $I_{corr}$ (μA.mm$^{-2}$) | $E_{transition}$ (mV) | $I_{passive}$ (μA.mm$^{-2}$) |
|---|---|---|---|---|
| LPBF-1 μm | −212 | 1.6E-4 | 486 | 0.067 |
| CONV-1 μm | −199 | 9.6E-4 | 387 | 0.128 |
| LPBF-1200 Grit | −208 | 6.2E-4 | 593 | 0.135 |
| CONV-1200 Grit | −319 | 2.2E-4 | 197 | 0.133 |

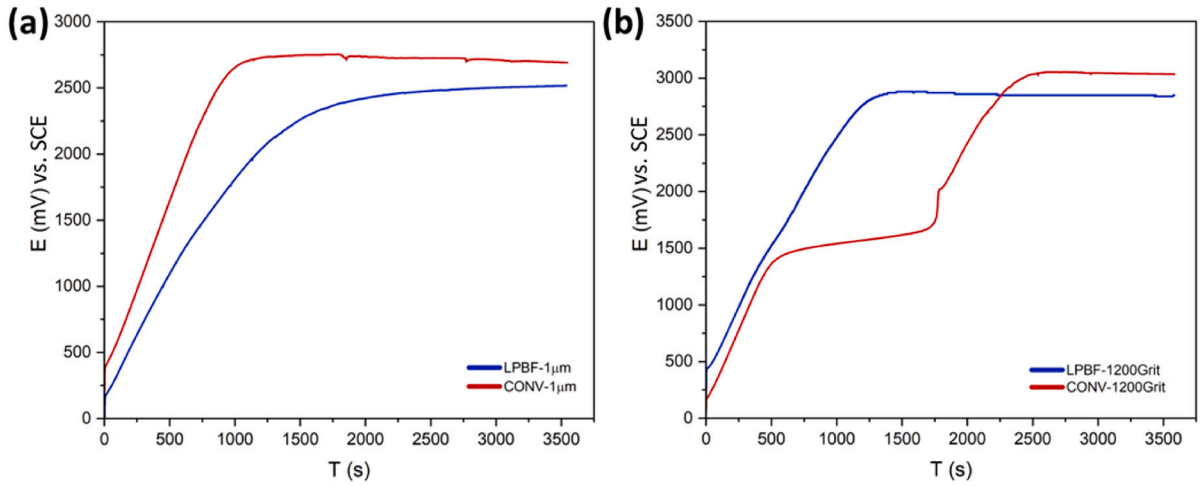


**Fig. 7.** Galvanostatic polarization under constat current density in the passive range for (a) 1 μm surface finish, and (b) for the specimens polished up to 1200 grit size.

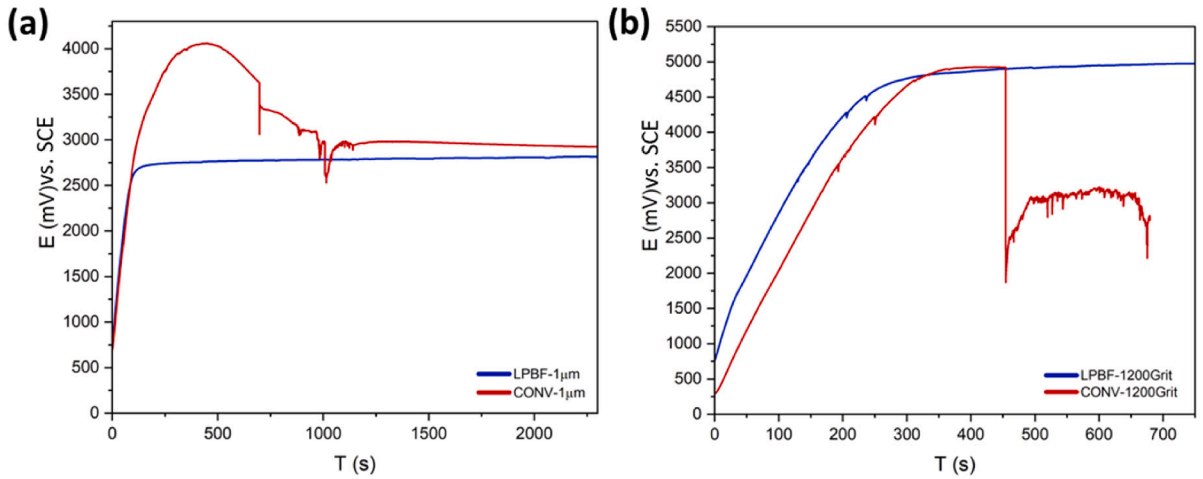


**Fig. 8.** Galvanostatic polarization under constat current density of 10 μA for (a) 1 μm surface finish, and (b) for the specimens polished up to 1200 grit size.

imperfections on the conventional surface could act as initiation sites for localized breakdown of the passive layer. Interestingly, even the L-PBF samples exhibited occasional breakdowns, although of a lesser magnitude and occurring at later times compared to the conventional samples. However, the L-PBF material demonstrates superior stability by exhibiting fewer and less severe breakdown events.

The results obtained with the 1200 Grit samples (Fig. 9b) were less conclusive due to the influence of surface roughness. The increased surface area associated with the rougher finish can significantly impact the measured current density. This makes it challenging to isolate the specific contribution of the material's intrinsic passive layer stability from the geometrical effects of surface roughness. The lower overall current density observed for the 1200 Grit samples compared to the 1 μm samples can be attributed to the larger surface area exposed to the electrolyte solution, leading to a more distributed current flow.

Overall, the potentiostatic polarization results reinforce the notion of a more stable passive layer formed on the L-PBF material compared to the conventional material. This finding aligns with the observations from the galvanostatic, EIS, and potentiodynamic polarization results and suggests that the L-PBF material exhibits superior resistance to breakdown under both constant current and constant potential conditions.

### *3.2.6. Stress-assisted electrochemical polarization in fluoride containing solution utilising microcapillary technique*

Electrochemical techniques have been a cornerstone of SCC studies, particularly in understanding the critical potential. For over two decades, these methods have been instrumental in detecting SCC propagation through potential and/or current density measurements [44]. However, a significant challenge in these methods lies in the large surface area exposed to the corrosive environment.

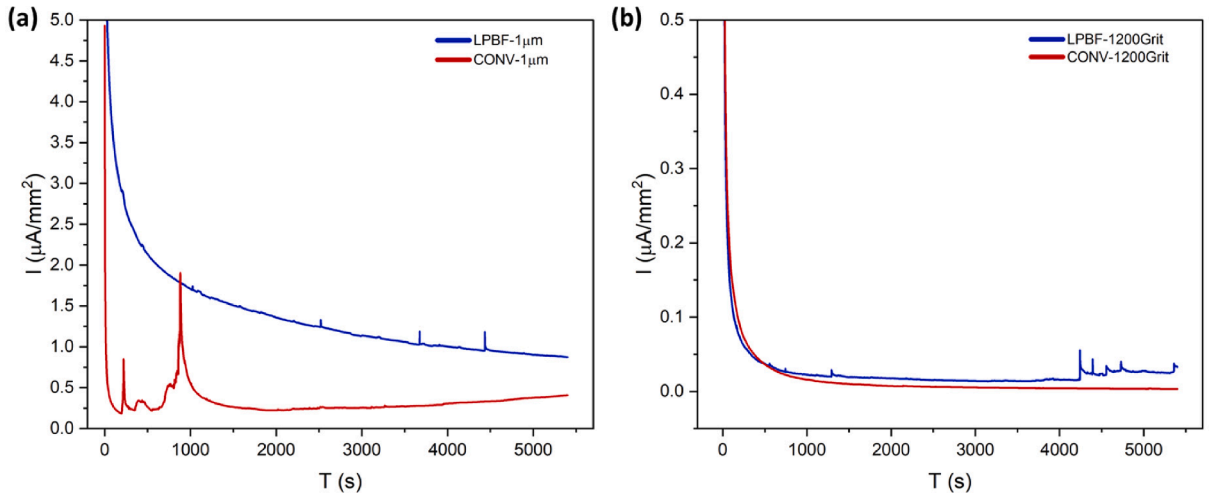


**Fig. 9.** Potentiostatic polarization behaviour of L-PBF and conventional alloy for (a) specimens polished up to 1 μm, and (b) 1200 grit size.

The localized nature of passive layer breakdown and/or SCC initiation sites makes their detection difficult for subsequent microstructural analysis. Reducing the investigated surface area can significantly enhance the early detection of SCC initiation sites compared to traditional methods.

The microcapillary technique, as demonstrated in various investigations, offers a promising approach for SCC initiation [24,25,45], and early stages of passive layer breakdown studies [23,28,46,47]. Conventional methods struggle to detect early-stage corrosion due to their reliance on large surface areas. Microcapillary technique, with its high sensitivity, can effectively identify subtle changes in the submicron structural state of materials, enabling early detection of SCC initiation and providing deeper insights into the initial stages of passive layer breakdown.

Microcapillary electrochemical polarization experiments were employed to investigate the combined effect of tensile strain and a fluoride-contaminated environment, representing the conditions encountered by dental implants in the oral cavity. This approach aimed to gain insights into the material's response to these combined stresses.

The OCP measurements under different loading conditions as shown in Fig. 10 reveals significant differences in the behaviour of L-PBF and conventional samples. The OCP of the conventional sample stabilized relatively quickly, suggesting a faster establishment of a certain level of passivity in this environment. The L-PBF material exhibited widespread instability, characterized by continuous breakdowns and repassivation events in the OCP curve. However, two distinct regions emerged where the OCP tended towards a certain value. In the time range between 800 and 2000 s, the L-PBF sample displayed lower OCP values compared to the conventional counterpart, indicating a less stable passive layer and potentially higher corrosion susceptibility. After 2500 s, The L-PBF OCP curve started oscillating around potential levels comparable to the conventional sample, suggesting a possible transition towards a more stable passive state with repeated breakdown-repassivation cycles. The presence of fluoride ions in the solution resulted in a significant decrease (approximately 700 mV) in the OCP values compared to those observed in SBF tests. This confirms the well-established ability of fluoride ions to exacerbate corrosion phenomena in titanium alloys [29–34].

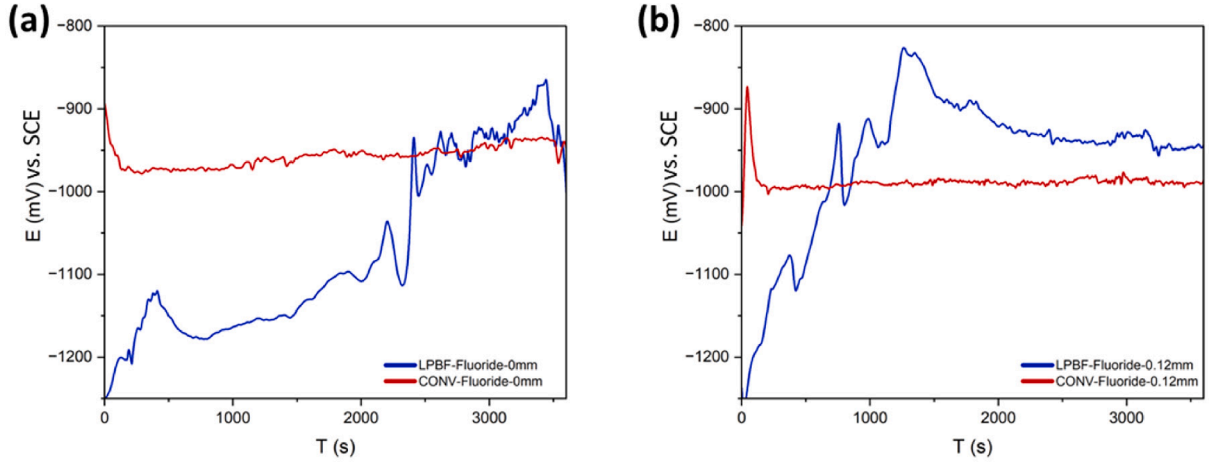


**Fig. 10.** OCP results for conventional and L-PBF specimens (a) in as-built state, and (b) under constant tensile straining.

The application of a mechanical load during the OCP measurement yielded further insights. While the L-PBF material under load stabilized at slightly higher OCP values compared to the unloaded case, it still exhibited a higher potential compared to the loaded conventional sample. This suggests that under static straining condition, the L-PBF material might possess inherently better corrosion resistance than the conventional material, even in the aggressive environment. The OCP curve of the conventional sample remained more stable even under applied stress, with the L-PBF counterpart requiring several repassivation events before reaching a stable state. This suggests a potentially superior ability of the conventional material to maintain a passive layer under mechanical load in this specific environment. The OCP data suggest that the L-PBF material typically exhibits corrosion resistance comparable to the conventionally produced alloy under static conditions. However, under stress conditions in Fluoride containing solution, the interplay between the L-PBF's superior mechanical properties (potentially due to its finer-grained microstructure) and its susceptibility to breakdown-repassivation events becomes crucial. It is possible that the combined effect of stress and breakdown events might temporarily compromise the L-PBF material's corrosion resistance, allowing the conventional sample to exhibit a more stable OCP response.

Furthermore, the potentiodynamic polarisation curves further elucidated the corrosion behaviour of the samples in the aggressive environment as shown in Fig. 11. The aggressive solution resulted in significantly higher average current densities compared to the SBF tests, indicating a more pronounced overall corrosion attack. Despite the challenging environment, both samples and under both load conditions managed to reach a passivation zone, characterized by a vertical region in the curve. This confirms the inherent ability of Ti6Al4V to form a protective passive layer even under aggressive conditions and applied stress. The Ecorr values were consistently lower in the conventional samples compared to the L-PBF material, by over 200 mV for both load conditions. Additionally, Ecorr for both materials further decreased with the application of stress. This suggests that the conventional material is inherently more susceptible to corrosion initiation in this environment, and this susceptibility is further worsened by the applied load. The transition region between the cathodic and anodic branches displayed lower current densities for the L-PBF samples at similar potentials. This indicates that the L-PBF material might experience less aggressive corrosion during the initial stages of film breakdown compared to the conventional material.

The samples under stress (Fig. 11b) exhibit distinct pitting regions in the transition zone around −500 mV. This suggests that localized acidification on the stressed surface facilitated the initiation and propagation of localized corrosion attack in both materials. Interestingly, even the unloaded conventional sample displayed signs of localized attack, highlighting the superior resistance of the L-PBF material under these specific conditions. Both materials reached anodic zones characterized by a vertical trend in the potentiodynamic curves, indicating the formation of a passive layer with similar current densities between −500 mV and 0 mV. However, some key differences emerged within the passivation zone. The current density in this region was lower for the undeformed samples compared to the loaded ones. This suggests that the applied stress might compromise the integrity of the passive layer, leading to a higher rate of passive film breakdown and repassivation events, reflected by the increased current flow. The conventional samples exhibited greater instability within the passivation zone, particularly for the stressed sample. This instability might be attributed to ongoing damage to the surface layer caused by localized corrosion, leading to breakdown-repassivation occurrence within the passive film. This highlights the potential vulnerability of the conventional material's passive layer under combined stress and aggressive environment conditions.

The overall potentiodynamic polarization analysis suggests comparable performance between the L-PBF and conventional materials in terms of achieving passivation in the aggressive environment. However, the L-PBF material exhibited superior corrosion resistance during the initial stages of film breakdown, as indicated by lower current densities in the transition region. The L-PBF material demonstrated a higher resistance to localized corrosion, particularly under static straining conditions, compared to the conventional material. This might be attributed to the finer-grained microstructure and potentially more robust passive layer

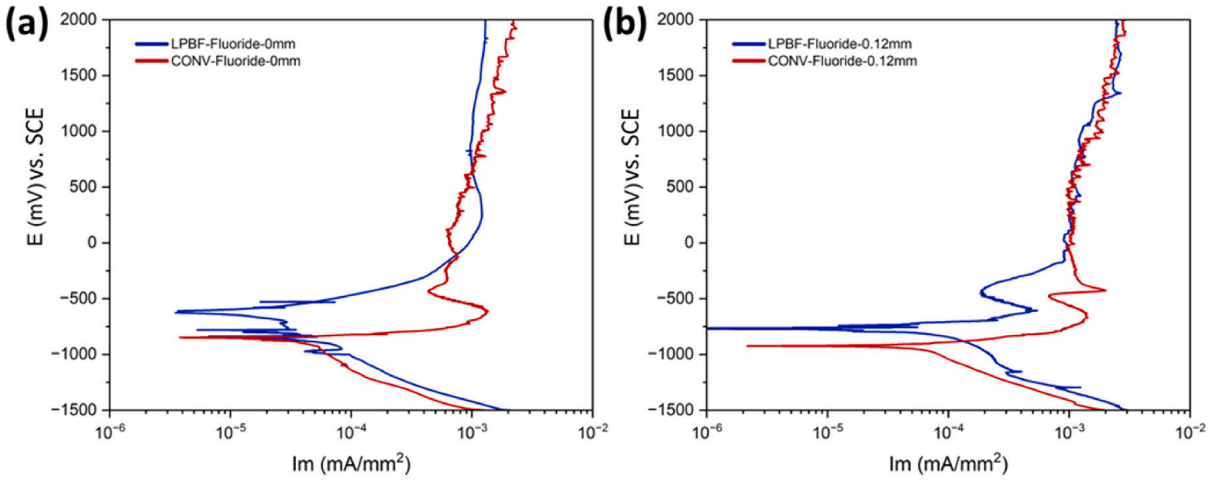


**Fig. 11.** Potentiodynamic polarization results for conventional and L-PBF specimens (a) in as-built state, and (b) under constant tensile straining.

formation on the L-PBF samples. Furthermore, the application of stress impacted both materials, promoting localized acidification and facilitating the initiation and propagation of localized corrosion attack. However, the conventional material appeared to be more significantly affected by the combined stress and aggressive environment, exhibiting higher overall current densities and greater instability within the passivation zone.

Furthermore, the galvanostatic polarization results obtained at various straining condition as shown in Fig. 12 reveals key insights into the performance of the L-PBF and conventional materials under controlled current conditions. For the unstrained samples (Fig. 12a), the potential-time curves for both materials exhibit a similar trend. However, the L-PBF curve consistently displayed a slightly higher potential compared to the conventional curve. According to Ohm's law [48], a higher potential at a fixed current density indicates a greater resistance to electron flow across the material's surface layer. This translates to a lower susceptibility to corrosion for the L-PBF material. This observation aligns with the findings from the macro-corrosion tests, suggesting that the L-PBF material possesses a superior passive layer for resisting corrosion in this aggressive environment.

Furthermore, the influence of applied deformation on the galvanostatic response varied depending on the deformation level. At deformation levels of 30 %, and 100 % (Fig. 12b, and d), the potential difference between the L-PBF and conventional curves become more pronounced. This suggests that the intrinsic differences in microstructure and passive layer properties between the materials play a more significant role in resisting corrosion under moderate stress conditions. At 60 % deformation level, the galvanostatic curves for the L-PBF and conventional materials exhibited minimal differences.

This observation suggests that the effect of applied stress on the passive layer might outweigh the intrinsic material differences at this deformation level. It is possible that the combined influence of stress and the aggressive environment overwhelms the subtle variations in passive layer properties between the materials as a consequence of internal residual stresses (which is inevitable in L-PBF processed materials) and the redistribution of stresses after tensile straining at 60 %. Under the highest applied deformation (Fig. 12d), the L-PBF material demonstrates a clearly better performance compared to conventional counterpart. The potential measured for the L-PBF sample significantly surpassed that of the conventional sample. This finding highlights the superior resistance of the L-PBF material's passive layer to the combined effects of high stress and a corrosive environment. This implies that the L-PBF material's

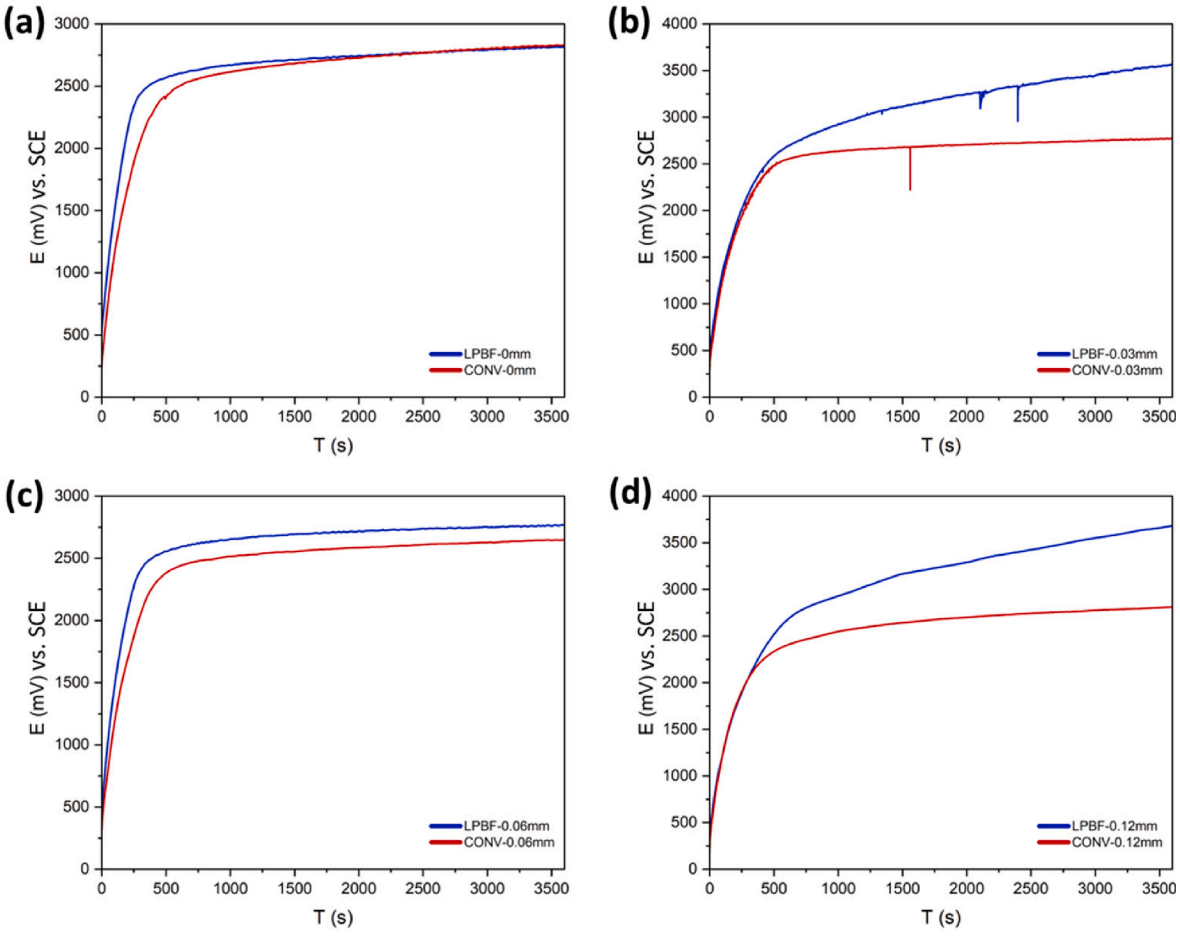


**Fig. 12.** Galvanostatic polarization results under various tensile straining corresponding to (a) as-built without strain, (b) 30%, (c) 60%, and (d) corresponding to 0.2% proof strain.

microstructure and potentially a thicker and more compact passive layer contribute to its enhanced performance under these extreme conditions. The superior performance of the L-PBF material's passive layer, as demonstrated in previous sections, could be attributed to the significantly finer grain size. This finer microstructure could facilitate enhanced ion diffusion (the reduced grain size could promote faster diffusion of essential ions involved in passive layer formation and repair towards the material's surface), and oxygen diffusion which the shorter diffusion distances within the finer grains might also facilitate the inward diffusion of oxygen, a crucial element for maintaining a robust oxide layer [49–52].

Consequently, this combined effect of enhanced diffusion processes could contribute to the formation of a more protective and stable passive layer on the L-PBF material compared to its conventionally processed counterpart. The utilization of the microcapillary technique offers a crucial advantage. Since the technique focuses on a small area of the material surface, the influence of surface finish or localized defects is minimized. This allows for a more isolated evaluation of the intrinsic properties of the passive layer formed on each material. The galvanostatic polarization test results provide strong evidence for the superior corrosion performance of the L-PBF material, particularly under stress conditions in the aggressive environment. The L-PBF material consistently exhibited a more stable and higher potential under constant current, indicating a more robust passive layer that effectively hinders electron flow and resists corrosion.

### *3.2.7. Corrosion morphology*

To elucidate the morphology of the corrosion attack on the sample surfaces after galvanostatic polarization in fluoride-containing SBF under 0.2 % proof strain, both optical microscopy and SEM analyses were conducted. As illustrated in Fig. 13, optical microscopy of the corroded zones formed during the microcapillary test reveals a distinct difference between the specimens. The conventionally processed material exhibited significantly higher levels of localized corrosion on its surface, displayed as larger and more numerous areas of attack. Conversely, the L-PBF specimen displayed only a few occasional signs of pitting corrosion, confirming the observed differences in the galvanostatic polarization results presented earlier in Fig. 12d.

This qualitative observation aligns with the trends observed in the polarization curves. The L-PBF material's superior performance in the galvanostatic tests is reflected in the minimal surface damage observed under optical microscopy. In contrast, the extensive localized attack on the conventional sample's surface signifies its increased susceptibility to corrosion under the synergistic effect of tensile straining and fluoride containing corrosive media.

Furthermore, SEM analysis was performed on the surfaces of conventional and L-PBF samples subjected to tensile strain corresponding to 0.2 % proof strain in SBF solution with fluoride content. As shown in Fig. 14, no sign of cracks within the corroded areas of either the SBF or the fluoride-enriched solution samples for both conventional and L-PBF materials. This suggests that neither materials experienced significant SCC under the applied strain and in these specific environments.

Although no evidence of SCC was identified, qualitative analysis of the surface morphology revealed distinct differences between the materials. Notably, the surfaces of the conventional samples exhibited a significantly higher degree of corrosion compared to their L-PBF counterparts. This observation suggests superior overall corrosion resistance for the L-PBF material. Furthermore, the SEM analysis served as a valuable tool to corroborate the differences in corrosion performance observed between the specimens, particularly those where microcapillary electrochemical polarization results had already indicated such disparities.

The SEM analysis provided further evidence for the superior performance of the L-PBF material, particularly under the maximum applied strain corresponding to proof strain. The L-PBF material exhibited less overall surface damage compared to the conventional material which can be attributed to several factors. The predominant presence of the martensitic phase in the L-PBF material makes it immune to the detrimental effects of galvanic couple corrosion observed in the conventional samples due to the alpha–beta phase combination. Additionally, the finer, needle-like grains in the L-PBF microstructure enhance its resistance to intergranular corrosion. Furthermore, the significantly smaller grain size observed in the L-PBF specimens compared to their conventionally processed

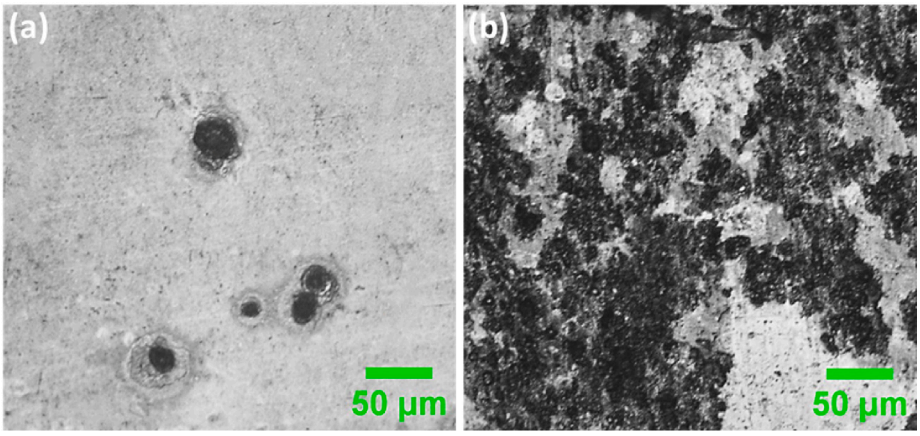


**Fig. 13.** Optical micrographs of corroded microcapillary zone after galvanostatic polarization in fluoride containing sbf under tensile straining corresponding to 0.2 % proof strain for (a) L-PBF Ti6Al4V alloy, and (b) for the conventional counterpart.

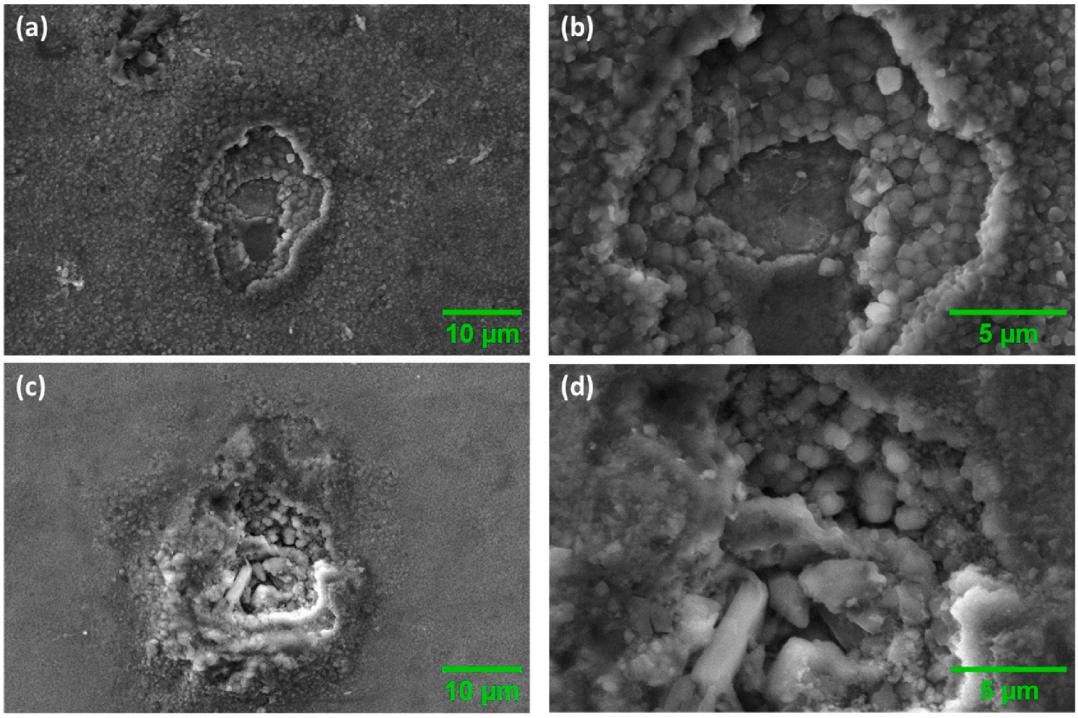


**Fig. 14.** SEM analysis of the pits after microcapillary galvanostatic polarization in fluoride containing SBF solution under tensile straining corresponding to 0.2 % proof strain for (a), and (b) LPBD Ti6Al4V, and (c), and (d) for conventional specimen.

counterparts is likely to contribute to enhanced diffusion, ultimately leading to a more robust passive layer. The finer grain structure facilitates faster diffusion of ions, both inwards from the environment (oxygen) and outwards (metal ions) from the bulk material. This includes oxygen ions, which are critical for the formation and repair of the passive layer, as well as metal ions that contribute to the passive layer's composition. Enhanced diffusion of these ions promotes faster and more efficient (more compact) passive layer formation on the L-PBF material's surface.

Combined, these diffusion-related benefits associated with the finer grain size in the L-PBF specimens contribute to the formation of a more compact and robust passive layer compared to the conventional material. The susceptibility of the conventional material to pitting corrosion, particularly under conditions of lower pH as evidenced by the SEM analysis, corresponds with the findings reported by Yang et al. [53]. Their research highlighted the role of intergranular and galvanic corrosion involving the alpha and beta phases in conventional Ti6Al4V, where the alpha phase exhibited lower corrosion resistance. The SEM analysis presented here provides further visual evidence supporting this mechanism.

The primary objective of this study was to elucidate the intrinsic microstructural effects of L-PBF on corrosion performance and to compare these findings with conventionally produced Ti6Al4V alloys. This investigation represents one of the initial steps in understanding how the microstructural characteristics of L-PBF processed materials influence corrosion behaviour, using microcapillary electrochemical techniques with and without tensile loading. While the potential impact of build direction on corrosion performance is a compelling area for exploration, it was beyond the scope of this study. Future research could offer deeper insights into how passive layer performance varies with different build directions and process parameters specific to the L-PBF process.

## 4. Conclusion

This study thoroughly examined the corrosion behaviour of Ti6Al4V alloy produced by Laser Powder Bed Fusion (L-PBF) compared to conventionally manufactured equivalents. The key findings can be summarized as follows:

- The microcapillary electrochemical method effectively identified minor variations in the corrosion performance of L-PBF and conventional materials, both with and without tensile strain.
- Conventional material showed a biphasic microstructure with alpha phase grains in a beta matrix, whereas L-PBF samples had a uniform martensitic alpha' phase with a fine, needle-like grain structure.
- L-PBF material exhibited superior corrosion resistance due to a stable, resistant, and rapidly forming passive layer, unlike the more susceptible passive layer on conventional samples.
- Polished samples (1200 Grit) indicated that surface roughness significantly influenced corrosion behaviour over microstructural differences.

- Under tensile strain, the L-PBF alloy showed markedly improved corrosion resistance over conventional material, attributed to its finer grain size and submicron martensitic structure.
- High fluoride ion concentrations in the solution worsened corrosion compared to simulated body fluid solutions, with conventional Ti6Al4V more prone to pitting corrosion.
- Both conventional and L-PBF samples demonstrated excellent resistance to stress corrosion cracking, with no cracks observed even under high deformation in corrosive environments.

## CRediT authorship contribution statement

**Arshad Yazdanpanah:** Writing – review & editing, Writing – original draft, Visualization, Validation, Software, Methodology, Investigation, Formal analysis, Data curation, Conceptualization. **Nicolò Capuzzo:** Writing – original draft, Visualization, Investigation, Data curation. **Mona Khodabakhshi:** Writing – original draft, Visualization, Software, Investigation, Formal analysis, Data curation. **Manuele Dabalà:** Writing – review & editing, Supervision, Project administration, Funding acquisition, Conceptualization.

## Declaration of competing interest

The authors declare that they have no known competing financial interests or personal relationships that could have appeared to influence the work reported in this paper.

## Data availability

Data will be made available on request.

## Acknowledgement

This work was supported by the University of Padova, Department of Industrial Engineering.

## References

[1] C.H. Lloyd, S.N. Scrimgeour, D. Brown, R.L. Clarke, R.V. Curtis, P.V. Hatton, A.J. Ireland, J.F. McCabe, J.W. Nicholson, J.C. Setcos, M. Sherriff, R. van Noort, D. C. Watts, C.J. Whitters, D. Wood, Dental materials: 1995 literature review, J. Dent. 25 (1997) 173–208. doi: 10.1016/S0300-5712(96)00077-2.
[2] F.H. Jones, Teeth and bones: applications of surface science to dental materials and related biomaterials, Surf. Sci. Rep. 42 (2001) 75–205, https://doi.org/10.1016/S0167-5729(00)00011-X.
[3] C.T. Laurencin, A.M.A. Ambrosio, M.D. Borden, J.A.C. Jr, Tissue Engineering: Orthopedic Applications, Annu. Rev. Biomed. Eng. 1 (1999) 19–46, https://doi.org/10.1146/annurev.bioeng.1.1.19.
[4] S. Gialanella, A. Malandruccolo, Titanium and Titanium Alloys, in: S. Gialanella, A. Malandruccolo (Eds.), Aerosp. Alloys, Springer International Publishing, Cham, 2020: pp. 129–189. doi: 10.1007/978-3-030-24440-8_4.
[5] M. Niinomi, M. Nakai, J. Hieda, Development of new metallic alloys for biomedical applications, Acta Biomater. 8 (2012) 3888–3903, https://doi.org/10.1016/j.actbio.2012.06.037.
[6] E. Marin, A. Lanzutti, Biomedical Applications of Titanium Alloys: A Comprehensive Review, Materials 17 (2024) 114, https://doi.org/10.3390/ma17010114.
[7] T. DebRoy, H.L. Wei, J.S. Zuback, T. Mukherjee, J.W. Elmer, J.O. Milewski, A.M. Beese, A. Wilson-Heid, A. De, W. Zhang, Additive manufacturing of metallic components – Process, structure and properties, Prog. Mater. Sci. 92 (2018) 112–224, https://doi.org/10.1016/j.pmatsci.2017.10.001.
[8] Review of laser powder bed fusion (LPBF) fabricated Ti-6Al-4V: process, post-process treatment, microstructure, and property, (n.d.). https://www.light-am.com/en/article/doi/10.37188/lam.2021.020 (accessed July 8, 2024).
[9] J. Giannatsis, V. Dedoussis, Additive fabrication technologies applied to medicine and health care: a review, Int. J. Adv. Manuf. Technol. 40 (2009) 116–127, https://doi.org/10.1007/s00170-007-1308-1.
[10] S.K. Sinha, Chapter 5 - Additive manufacturing (AM) of medical devices and scaffolds for tissue engineering based on 3D and 4D printing, in: K.K. Sadasivuni, K. Deshmukh, M.A. Almaadeed (Eds.), 3D 4D Print. Polym. Nanocomposite Mater., Elsevier, 2020: pp. 119–160. doi: 10.1016/B978-0-12-816805-9.00005-3.
[11] D.D. Gu, W. Meiners, K. Wissenbach, R. Poprawe, Laser additive manufacturing of metallic components: materials, processes and mechanisms, Int. Mater. Rev. 57 (2012) 133–164, https://doi.org/10.1179/1743280411Y.0000000014.
[12] S. Liu, Y.C. Shin, Additive manufacturing of Ti6Al4V alloy: A review, Mater. Des. 164 (2019) 107552, https://doi.org/10.1016/j.matdes.2018.107552.
[13] S. Hosseini, S. Mirdamadi, A. Nemati, Porous Ti6Al4V scaffolds for dental implants: Microstructure, mechanical, and corrosion behavior, Proc. Inst. Mech. Eng. Part J. Mater. Des. Appl. 230 (2016) 927–933. doi: 10.1177/1464420715588218.
[14] P. Chandramohan, S. Bhero, B.A. Obadele, P.A. Olubambi, Laser additive manufactured Ti–6Al–4V alloy: tribology and corrosion studies, Int. J. Adv. Manuf. Technol. 92 (2017) 3051–3061, https://doi.org/10.1007/s00170-017-0410-2.
[15] H.M. Hamza, K.M. Deen, W. Haider, Microstructural examination and corrosion behavior of selective laser melted and conventionally manufactured Ti6Al4V for dental applications, Mater. Sci. Eng. C 113 (2020) 110980, https://doi.org/10.1016/j.msec.2020.110980.
[16] A. Sharma, M.C. Oh, J.-T. Kim, A.K. Srivastava, B. Ahn, Investigation of electrochemical corrosion behavior of additive manufactured Ti–6Al–4V alloy for medical implants in different electrolytes, J. Alloys Compd. 830 (2020) 154620, https://doi.org/10.1016/j.jallcom.2020.154620.
[17] T.-M. Chiu, M. Mahmoudi, W. Dai, A. Elwany, H. Liang, H. Castaneda, Corrosion assessment of Ti-6Al-4V fabricated using laser powder-bed fusion additive manufacturing, Electrochimica Acta 279 (2018) 143–151, https://doi.org/10.1016/j.electacta.2018.04.189.
[18] L.-Y. Chen, H.-Y. Zhang, C. Zheng, H.-Y. Yang, P. Qin, C. Zhao, S. Lu, S.-X. Liang, L. Chai, L.-C. Zhang, Corrosion behavior and characteristics of passive films of laser powder bed fusion produced Ti–6Al–4V in dynamic Hank's solution, Mater. Des. 208 (2021) 109907, https://doi.org/10.1016/j.matdes.2021.109907.
[19] N. Dai, L.-C. Zhang, J. Zhang, Q. Chen, M. Wu, Corrosion behavior of selective laser melted Ti-6Al-4 V alloy in NaCl solution, Corros. Sci. 102 (2016) 484–489, https://doi.org/10.1016/j.corsci.2015.10.041.
[20] S. Tamilselvi, V. Raman, N. Rajendran, Corrosion behaviour of Ti–6Al–7Nb and Ti–6Al–4V ELI alloys in the simulated body fluid solution by electrochemical impedance spectroscopy, Electrochimica Acta 52 (2006) 839–846, https://doi.org/10.1016/j.electacta.2006.06.018.
[21] X. Chen, Q. Liao, M. Gong, Q. Fu, Corrosion Performances of Selective Laser Melting Ti6Al4V Alloy in Different Solutions, Metals 13 (2023) 192, https://doi.org/10.3390/met13020192.
[22] A. Yazdanpanah, M. Franceschi, P. Rebesan, M. Dabalà, Correlation of Lack of Fusion Pores with Stress Corrosion Cracking Susceptibility of L-PBF 316L: Effect of Surface Residual Stresses, Materials 15 (2022) 7151, https://doi.org/10.3390/ma15207151.

[23] A. Yazdanpanah, R.I. Revilla, M. Franceschi, A. Fabrizi, S. Khademzadeh, M. Khodabakhshi, I. De Graeve, M. Dabalà, Unveiling the impact of laser power variations on microstructure, corrosion, and stress-assisted surface crack initiation in laser powder bed fusion-processed Ni-Fe-Cr alloy 718, Electrochimica Acta 476 (2024) 143723, https://doi.org/10.1016/j.electacta.2023.143723.
[24] C. Gasparrini, J.O. Douglas, A. Yazdanpanah, R. Stroud, G. Divitini, M. Dabalà, G.G. Scatigno, S. Pedrazzini, M.R. Wenman, D. Badocco, P. Pastore, N. Terranova, G. Mariano, F. Dacquait, M.D. Palma, R. Villari, P. Sonato, Corrosion of 316L exposed to highly concentrated borated water used as shield in nuclear fusion experimental reactors cooling circuits, Corros. Sci. 230 (2024) 111902, https://doi.org/10.1016/j.corsci.2024.111902.
[25] A. Yazdanpanah, F.R. Biglari, A. Fallahi Arezoodar, M. Dabalà, Role of grinding induced surface residual stress on probability of stress corrosion cracks initiation in 316L austenitic stainless steel in 3.5% sodium chloride aqueous solution, Corros. Eng. Sci. Technol. 56 (2021) 81–92. doi: 10.1080/1478422X.2020.1812818.
[26] F. Andreatta, L. Fedrizzi, The use of the electrochemical micro-cell for the investigation of corrosion phenomena, Electrochimica Acta 203 (2016) 337–349, https://doi.org/10.1016/j.electacta.2016.01.099.
[27] F. Mariani, I. Gualandi, W. Schuhmann, E. Scavetta, Micro- and nano-devices for electrochemical sensing, Microchim. Acta 189 (2022) 459, https://doi.org/10.1007/s00604-022-05548-3.
[28] A. Yazdanpanah, G. Pagot, M. Franceschi, P. Rebesan, M. Venturin, J. Botinha, B. Gerhmann, I. De Graeve, V.D. Noto, R.I. Revilla, M. Dabalà, Mechanism of alteration in passivity of additively manufactured Ni-Fe-Cr Alloy 718 caused by minor carbon variation, Electrochimica Acta (2024) 144925. doi: 10.1016/j.electacta.2024.144925.
[29] E.J. Kassab, J.P. Gomes, Assessment of nickel titanium and beta titanium corrosion resistance behavior in fluoride and chloride environments, Angle Orthod. 83 (2013) 864–869, https://doi.org/10.2319/091712-740.1.
[30] B. Lindholm-Sethson, B. i. Ardlin, Effects of pH and fluoride concentration on the corrosion of titanium, J. Biomed. Mater. Res. A 86A (2008) 149–159. doi: 10.1002/jbm.a.31415.
[31] X. Li, L. Wang, L. Fan, M. Zhong, L. Cheng, Z. Cui, Understanding the effect of fluoride on corrosion behavior of pure titanium in different acids, Corros. Sci. 192 (2021) 109812, https://doi.org/10.1016/j.corsci.2021.109812.
[32] S. Takemoto, M. Hattori, M. Yoshinari, E. Kawada, Y. Oda, Corrosion behavior and surface characterization of titanium in solution containing fluoride and albumin, Biomaterials 26 (2005) 829–837, https://doi.org/10.1016/j.biomaterials.2004.03.025.
[33] Corrosion Behavior of Pure Titanium and Titanium Alloys in Fluoride-containing Solutions, (n.d.). https://www.jstage.jst.go.jp/article/dmj1982/20/4/20_4_305/_article/-char/ja/ (accessed July 10, 2024).
[34] N. Schiff, B. Grosgogeat, M. Lissac, F. Dalard, Influence of fluoride content and pH on the corrosion resistance of titanium and its alloys, Biomaterials 23 (2002) 1995–2002, https://doi.org/10.1016/S0142-9612(01)00328-3.
[35] Y. Fan, W. Tian, Y. Guo, Z. Sun, J. Xu, Relationships among the Microstructure, Mechanical Properties, and Fatigue Behavior in Thin Ti6Al4V, Adv. Mater. Sci. Eng. 2016 (2016) 7278267, https://doi.org/10.1155/2016/7278267.
[36] F.I. Jamhari, F.M. Foudzi, M.A. Buhairi, A.B. Sulong, N.A. Mohd Radzuan, N. Muhamad, I.F. Mohamed, N.H. Jamadon, K.S. Tan, Influence of heat treatment parameters on microstructure and mechanical performance of titanium alloy in LPBF: A brief review, J. Mater. Res. Technol. 24 (2023) 4091–4110, https://doi.org/10.1016/j.jmrt.2023.04.090.
[37] P. Chandramohan, Laser additive manufactured Ti-6Al-4V alloy: Texture analysis, Mater. Chem. Phys. 226 (2019) 272–278, https://doi.org/10.1016/j.matchemphys.2019.01.035.
[38] N. Sato, Some concepts of corrosion fundamentals, Corros. Sci. 27 (1987) 421–433, https://doi.org/10.1016/0010-938X(87)90086-2.
[39] K.D. Ralston, N. Birbilis, Effect of Grain Size on Corrosion: A Review, Corrosion 66 (2010) 075005-075005–13. doi: 10.5006/1.3462912.
[40] A. Toloei, V. Stoilov, D. Northwood, The Relationship Between Surface Roughness and Corrosion, American Society of Mechanical Engineers Digital Collection (2014), https://doi.org/10.1115/IMECE2013-65498.
[41] G.S. Frankel, Fundamentals of Corrosion Kinetics, in: A.E. Hughes, J.M.C. Mol, M.L. Zheludkevich, R.G. Buchheit (Eds.), Act. Prot. Coat. New-Gener. Coat, Met., Springer, Netherlands, Dordrecht, 2016, pp. 17–32, https://doi.org/10.1007/978-94-017-7540-3_2.
[42] G.P. Power, W.P. Staunton, I.M. Ritchie, Mixed potential measurements in the elucidation of corrosion mechanisms—II Some Measurements, Electrochim. Acta 27 (1982) 165–169, https://doi.org/10.1016/0013-4686(82)80076-5.
[43] S. Choudhary, V. Cruz, A. Pandey, S. Thomas, N. Birbilis, Element-resolved electrochemical analysis of the passivity of additively manufactured stainless steel 316L, Corros. Sci. 189 (2021) 109576, https://doi.org/10.1016/j.corsci.2021.109576.
[44] P.L. Andresen, 5 - Understanding and predicting stress corrosion cracking (SCC) in hot water, in: D. Féron, R.W. Staehle (Eds.), Stress Corros. Crack. Nickel Based Alloys Water-Cool. Nucl. React, Woodhead Publishing, 2016, pp. 169–238, https://doi.org/10.1016/B978-0-08-100049-6.00005-7.
[45] M.S. Breimesser, S. Ritter, H.-P. Seifert, T. Suter, S. Virtanen, A New Approach towards the Characterization of IG SCC of Austenitic Stainless Steel by the Electrochemical Microcapillary Technique, ECS, Meet. Abstr. MA2011-02 (2011) 1694, https://doi.org/10.1149/MA2011-02/22/1694.
[46] A. Yazdanpanah, M. Franceschi, R.I. Revilla, S. Khademzadeh, I. De Graeve, M. Dabalà, Revealing the stress corrosion cracking initiation mechanism of alloy 718 prepared by laser powder bed fusion assessed by microcapillary method, Corros. Sci. 208 (2022) 110642, https://doi.org/10.1016/j.corsci.2022.110642.
[47] A. Yazdanpanah, L. Pezzato, M. Dabalà, Stress corrosion cracking of AISI 304 under chromium variation within the standard limits: Failure analysis implementing microcapillary method, Eng. Fail. Anal. 142 (2022) 106797, https://doi.org/10.1016/j.engfailanal.2022.106797.
[48] T. Levy-Nathansohn, Studies of the generalized Ohm's law, Phys. Stat. Mech. Its Appl. 241 (1997) 166–172, https://doi.org/10.1016/S0378-4371(97)00077-0.
[49] N.N. Aung, W. Zhou, Effect of grain size and twins on corrosion behaviour of AZ31B magnesium alloy, Corros. Sci. 52 (2010) 589–594, https://doi.org/10.1016/j.corsci.2009.10.018.
[50] K.D. Ralston, J.G. Brunner, S. Virtanen, N. Birbilis, Effect of Processing on Grain Size and Corrosion of AA2024-T3, Corrosion 67 (2011) 105001-105001–10. doi: 10.5006/1.3647762.
[51] L. Qin, J. Lian, Q. Jiang, Effect of grain size on corrosion behavior of electrodeposited bulk nanocrystalline Ni, Trans. Nonferrous Met. Soc. China 20 (2010) 82–89, https://doi.org/10.1016/S1003-6326(09)60101-1.
[52] K.D. Ralston, D. Fabijanic, N. Birbilis, Effect of grain size on corrosion of high purity aluminium, Electrochimica Acta 56 (2011) 1729–1736, https://doi.org/10.1016/j.electacta.2010.09.023.
[53] J. Yang, Y. Song, K. Dong, E.-H. Han, Research progress on the corrosion behavior of titanium alloys, Corros. Rev. 41 (2023) 5–20, https://doi.org/10.1515/corrrev-2022-0031.